

Microscopic treatment of energy partition in fission

M. Albertsson,¹ B.G. Carlsson,¹ T. Døssing,² P. Möller,^{1,3,4} J. Randrup,⁵ and S. Åberg¹

¹*Mathematical Physics, Lund University, S-221 00 Lund, Sweden*

²*Niels Bohr Institute, DK-2100 Copenhagen Ø, Denmark*

³*Theoretical Division, Los Alamos National Laboratory, Los Alamos, New Mexico 87545, USA*

⁴*P. Moller Scientific Computing and Graphics, Inc., Los Alamos, New Mexico 87544, USA*

⁵*Nuclear Science Division, Lawrence Berkeley National Laboratory, Berkeley, California 94720, USA*

(Dated: June 18, 2021)

The transformation of an atomic nucleus into two excited fission fragments is modeled as a strongly damped evolution of the nuclear shape, until scission occurs at a small critical neck radius, at which point the mass, charge, and shape of each fragment are extracted. The available excitation energy then is divided statistically on the basis of the microscopic level densities. This approach takes account of the important (and energy-dependent) finite-size effects. After the fragments have been fully accelerated and their shapes have relaxed to their equilibrium form, they undergo sequential neutron evaporation. The dependence of the resulting mean neutron multiplicity on the fragment mass, $\bar{\nu}(A)$, including the dependence on the initial excitation energy of the fissioning compound nucleus, is in good agreement with the observed behavior, as demonstrated here for $^{235}\text{U}(n,f)$.

Even 80 years after its discovery [1, 2], nuclear fission remains a fertile topic for experimental and theoretical research [3–6] and improvements in instrumentation, modeling, and computation have enabled a renaissance in the field.

In their seminal paper [7], Bohr and Wheeler described fission as an evolution of the nuclear shape subject to both conservative forces from the potential energy of deformation and dissipative forces resulting from the coupling to the residual system. This conceptually simple picture suggests that the shape dynamics can be regarded as a Brownian process, as pioneered by Kramers [8]. In the idealized limit of strong dissipation, the shape evolution can then be simulated by a random walk [9, 10] on the multi-dimensional potential-energy surface, from near the ground state shape, across the barrier region, until the system divides into two fragments at scission.

In a recent study [11], it was shown that the use of shape-dependent microscopic level densities for guiding the Brownian shape evolution provides a consistent (and parameter-free) framework for calculating the energy-dependent fission-fragment mass distribution.

We develop that approach further by partitioning the available excitation energy at scission between the two nascent fragments based on their microscopic level densities. The division of the available energy between the two fragments has long been puzzling because it appears to differ from expectations based on their masses. However, it was recently pointed out [12] that previous treatments [13–15] employed the simplified Fermi-gas (Bethe) formula [16] which may not be accurate at low energies where structure effects tend to be significant.

We demonstrate that a consistent use of the appropriate microscopic level densities in the distorted pre-fragments at scission leads to a remarkably good reproduction of the experimental data.

In our study, we generate and analyze a large number of scission configurations (typically 10^6) for the compound system $^{236}\text{U}^*$ having a specified initial excita-

tion energy E_0^* . For this task, we employ the Brownian shape evolution method [9], performing Metropolis walks on the potential-energy surface tabulated for the three-quadratic-surfaces shape family [17]. These shapes [18] are characterized by five parameters: the overall elongation given by the quadrupole moment Q , the radius c of the hyperbolic neck between the two spheroidal end sections which have deformations ε_1 and ε_2 , and the mass asymmetry α . Each Metropolis walk is started near the second minimum and continued across and beyond the outer barrier until the neck radius c has become smaller than the specified critical value $c_0=1.5$ fm.

At scission, the value of the asymmetry parameter α determines the mass numbers of the nascent heavy and light fragments, A_H and A_L . The associated charge numbers, Z_H and Z_L , are selected as those values that best preserve the $N:Z$ ratio. (For simplicity, we consider only divisions into even-even fragments in this first exploratory study.) Furthermore, the ε parameters give the spheroidal deformations of the nascent fragments, $\varepsilon_i^{\text{sc}}$, $i = H, L$. These generally differ from the corresponding ground-state deformations, $\varepsilon_i^{\text{gs}}$. The associated distortion energies, $E_i^{\text{dist}} = M_i(\varepsilon_i^{\text{sc}}) - M_i(\varepsilon_i^{\text{gs}})$, are converted into statistical fragment excitations later on as the fragment shapes relax to their ground-state forms. (Strictly speaking, a fragment acquires the equilibrium shape dictated by its degree of excitation, $\varepsilon_i^{\text{eq}}$, but the difference between that and $\varepsilon_i^{\text{gs}}$ is small and is ignored here.) The shape-dependent fragment masses, $M_i(\varepsilon)$, are calculated in the same microscopic-macroscopic model that was used to obtain the potential-energy surfaces [19].

Because (by assumption) the collective kinetic energy associated with the shape evolution is negligible prior to scission, the available excitation energy at scission is the difference between the total energy, E_{tot} , and the potential energy of the scission configuration,

$$E_{\text{sc}}^* = E_{\text{tot}} - U(Q_{\text{sc}}, c_{\text{sc}}, \varepsilon_1^{\text{sc}}, \varepsilon_2^{\text{sc}}, \alpha_{\text{sc}}). \quad (1)$$

In the present study, we assume that this quantity is

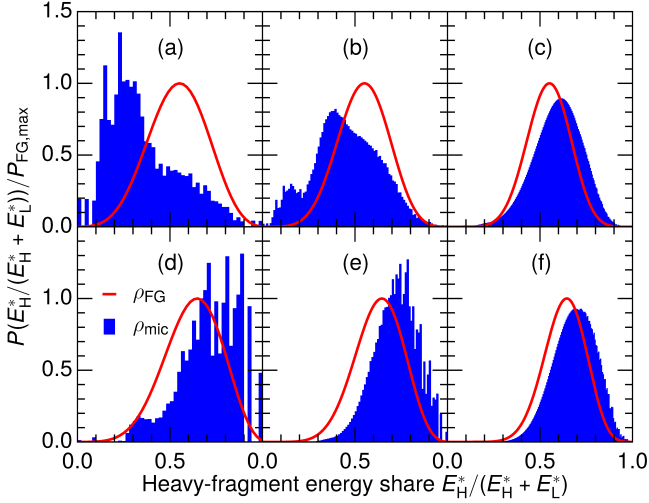


FIG. 1 (color online). The distribution function $P(E_H^*; E_{sc}^*)$ for the total excitation of the heavy fragment in $^{235}\text{U}(n, f)$ for two different divisions, either $(N, Z, \varepsilon)_H = (80, 50, -0.1)$ and $(N, Z, \varepsilon)_L = (64, 42, 0.3)$ (top panels) or $(N, Z, \varepsilon)_H = (92, 60, 0.1)$ and $(N, Z, \varepsilon)_L = (52, 32, 0.1)$ (bottom panels), and three different values of the available energy at scission, $E_{sc}^* = 10$ (left column), 20 (center column), 40 (right column) MeV. The distributions obtained from microscopic (blue histograms) and Fermi-gas (solid red curves) level densities are normalized to the maximum value of the Fermi-gas result.

divided statistically between the two fragments, *i.e.* the total excitation energy of the heavy fragment, E_H^* , is governed by the following microcanonical distribution,

$$P(E_H^*; E_{sc}^*) \sim \tilde{\rho}_H(E_H^*; \varepsilon_H^{sc}) \tilde{\rho}_L(E_{sc}^* - E_H^*; \varepsilon_L^{sc}), \quad (2)$$

and $E_L^* = E_{sc}^* - E_H^*$ due to energy conservation, where $\tilde{\rho}_i(E_i^*; \varepsilon_i^{sc}) \equiv \tilde{\rho}(N_i, Z_i, E_i^*; \varepsilon_i)$ is the effective density of states (see below) of a nucleus with neutron and proton numbers N_i and Z_i , spheroidal deformation ε_i , and a total excitation energy of E_i^* , with $i = H, L$.

The key novelty of the present study is the use of shape-dependent microscopic level densities in the above expression (2) for the partitioning of the available energy. The fragment level densities are calculated using the combinatorial model of Ref. [20], using the same model as that giving the shape-dependent compound nuclear level density employed in the Metropolis walk. Thus, for each emerging fragment, the neutron and proton wave functions are calculated in the spheroidal effective field and the many-quasi-particle excitations are constructed. For each such configuration, a pairing calculation is carried out and the associated rotational band is built. For each value of the angular momentum I , the level density $\rho(E^*, I; \varepsilon^{sc})$ is then extracted by counting the number of energy levels having angular momentum I in a small energy interval around E^* . In the present study, we are interested in the energy distribution only, so we sum over the fragment angular momentum, I_i , to obtain

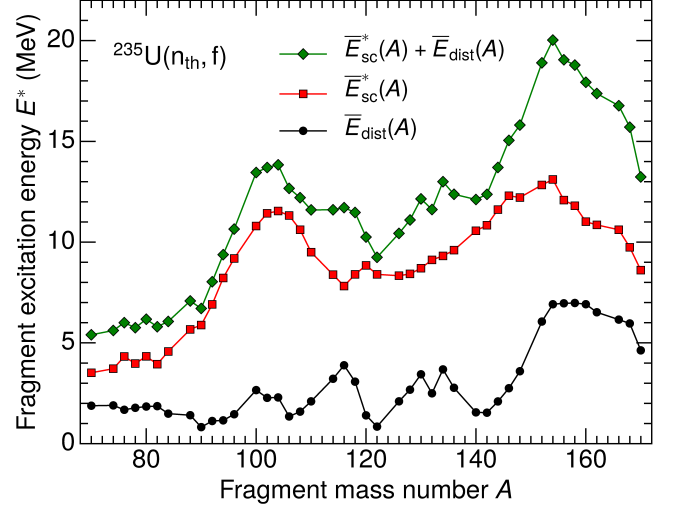


FIG. 2 (color online). As functions of the fragment mass number A are shown the mean fragment distortion energy $E_{\text{dist}}(A)$ (black dots), the mean excitation energy at scission, $E_{sc}^*(A)$ (red squares), and the sum, $E_{\text{dist}}(A) + E_{sc}^*(A)$ (green diamonds), as extracted from an ensemble of 10^6 scission configurations.

the effective density of states entering in Eq. (2),

$$\tilde{\rho}_i(E_i^*; \varepsilon_i^{sc}) = \sum_{I_i} (2I_i + 1) \rho_i(E_i^*, I_i; \varepsilon_i^{sc}). \quad (3)$$

Figure 1 shows the energy distribution $P(E_H; E_{sc}^*)$ at three different values of the total available energy E_{sc}^* for two different mass divisions having $(A_H:A_L) = (130:106)$ and $(152:84)$. These two divisions contribute to the yields at the inner and outer wings of the double-humped mass distribution, respectively, (see *e.g.* Fig. 9 of Ref. [11]), and the deformations considered are typical of those divisions.

The energy distribution was calculated with both the microscopic level density discussed above and a simplified Fermi-gas level density, $\rho_{\text{FG}}(E^*) \sim \exp[2\sqrt{aE^*}]$ with $a = A/(8 \text{ MeV})$. Both yield rather broad distributions due to the smallness of the nuclear system. The macroscopic form yields smooth Gaussian-like distributions peaked at $E_H^*/E_L^* = A_H/A_L$, whereas the microscopic form yields irregular distributions that may have qualitatively different appearances, especially at lower values of E_{sc}^* where quantal structure effects are most significant. In particular, it is possible that one fragment receives all the available energy with the partner fragment being left without excitation. Although the probability for this decreases quite rapidly with increasing E_{sc}^* , this feature is in dramatic contrast to the macroscopic result.

For the case shown in the top panel of Fig. 1, the heavy fragment is ^{130}Sn which is very close to being doubly magic. It therefore has a spherical ground-state shape, $\varepsilon_H^{\text{gs}} = 0$, while the light fragment, ^{106}Mo , has a well-deformed prolate ground-state shape, $\varepsilon_L^{\text{gs}} = 0.33$. The fragment deformations at scission are $\varepsilon_H^{sc} = -0.10$ and

$\varepsilon_L^{\text{sc}} = 0.30$ which both deviate only slightly from the ground-state deformations. The near magicity of the heavy fragment (with a shell correction energy of -10.2 MeV) causes the level density to remain very small up to excitation energies of 20 MeV. Conversely, the shell correction energy of the light fragment is $+0.35$ MeV and its level density is considerably larger than that of the heavy partner in that energy range. As a consequence, the energy distribution is peaked at small values of E_H^* and the major part of the energy goes to the light fragment. For example, when the total energy available for sharing is 10 MeV, the most likely outcome is that the heavy fragment receives only ≈ 2 MeV, while the light fragment gets ≈ 8 MeV. This is very different from the macroscopic (Fermi-gas) scenario in which the most likely excitations of those fragments are about 5.5 and 4.5 MeV, respectively.

The opposite appears when the two fragments differ more in size, as illustrated in the bottom panel of Fig. 1. Here the microscopic energy-partition distribution function strongly favors the heavy fragment, ^{152}Nd , relative to the light fragment, ^{84}Ge . In this case, the typical scission deformation of the heavy fragment is considerably smaller, $\varepsilon_H^{\text{sc}} = 0.10$, than its ground-state deformation, $\varepsilon_H^{\text{gs}} = 0.24$. Therefore the heavy fragment has a large single-particle level density and, consequently, it has a large positive shell correction, $+6.1$ MeV (as compared to -6.9 MeV for the ground-state shape) and a particularly high level density. On the other hand, the neutron number of the light fragment, $N_L = 52$, is close to being magic so its level density is low. As a result, the heavy fragment is strongly favored in the energy division, even up to quite high energies, as clearly seen in Fig. 1 (d)-(f).

As the available energy is increased, the microscopic energy partition distribution (2) approaches the macroscopic form obtained with the Fermi-gas level density [11] and the structure effects on the mass partition subside, albeit at various rates.

For each scission configuration obtained at the end of the Metropolis walk, the excitation energies of the nascent fragments are sampled from the appropriate microscopic partition distribution (2) illustrated in Fig. 1. For $^{235}\text{U}(n_{\text{th}}, f)$, the resulting mean excitation energy $\bar{E}_{\text{sc}}^*(A)$ is shown in Fig. 2 as a function of the fragment mass number A , together with the mean fragment distortion energy $\bar{E}_{\text{dist}}(A)$, as well as the sum of these two quantities which represents the total excitation energy of the fragment relative its ground state.

The mean fragment excitation energy at scission has a pronounced structure that may be qualitatively understood from the energy partition distribution functions of the two examples discussed above. The local minimum slightly below $A = 130$ and the local maximum around $A = 106$ result from the favoring of the light fragment in the energy sharing illustrated in Fig. 1 (a) – (c), while the pronounced maximum at $A \approx 150$ and the relatively low values in the $A \approx 84$ region result from the favoring of the heavy fragment illustrated in Fig. 1 (d) – (f).

With regard to the distortion energies, we note that

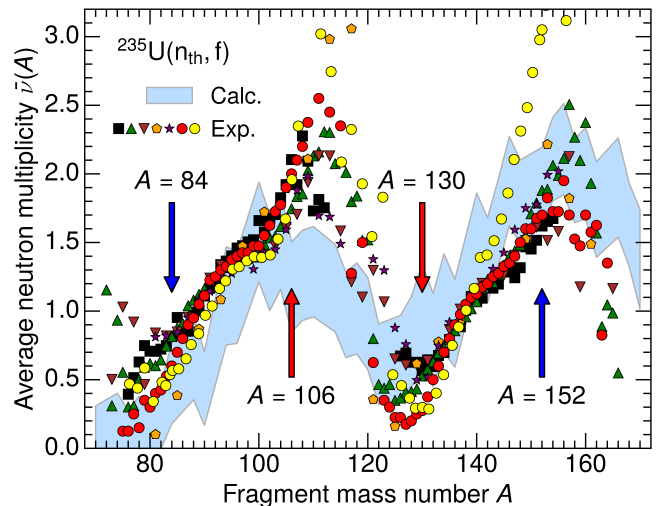


FIG. 3 (color online). For $^{235}\text{U}(n_{\text{th}}, f)$ the calculated mean neutron multiplicity as a function of the mass number of the primary fission fragment, $\bar{\nu}(A)$, is shown together with a variety of experimental data: black squares [21], yellow circles [22], green triangles [23], orange diamonds [24], purple stars [25] brown triangles [26], red circles [27]. The calculated values are at the center of the light-blue shaded band which has a width equal to the calculated dispersion of the neutron multiplicity distribution for that fragment mass, $\sigma_{\nu}(A)$. The red/blue arrows show the locations of the mass divisions selected in Fig. 1.

the scission shapes are typically less deformed than the corresponding ground-state shapes, $\varepsilon_i^{\text{sc}} < \varepsilon_i^{\text{gs}}$. The resulting mean distortion energies increase from 2 – 3 MeV for light fragments to 6 – 7 MeV for heavy fragments. As a consequence, the maximum in $\bar{E}_{\text{sc}}^*(A)$ around $A = 150$ is enhanced by the large distortion energies in the same mass region, as is clearly brought out in Fig. 2.

After a fragment has been fully accelerated and its shape has relaxed to its ground-state form, it disposes of its excitation energy by neutron evaporation and, on a longer time scale, by radiation of photons. Because the number of neutrons emitted reflects the degree of initial excitation, the dependence of the mean neutron multiplicity on the fragment mass, $\bar{\nu}(A)$, may be used to test the calculated energy partitioning. Therefore we consider neutron evaporation from the fragments.

Because the initial compound excitation energies are relatively low, neutron emission prior to (or during) fission is insignificant. Furthermore, the fragment angular momentum I is hardly affected by the evaporation, so the energy available for neutron evaporation is taken as $E = E^* - \bar{E}_{\text{rot}}$, where \bar{E}_{rot} is the average rotational energy (which will later contribute to the photon radiation). For a given fragment (Z, N, E, ε) , the kinetic energy ε_n of the evaporated neutron is sampled from the spectrum $\sim \bar{\rho}'(E'; \varepsilon') \varepsilon_n$, where $\bar{\rho}'$ denotes the effective level density in the daughter fragment $(Z' = Z, N' = N - 1, E' = E - \varepsilon_n - S_n, \varepsilon')$, with S_n being the neutron separation

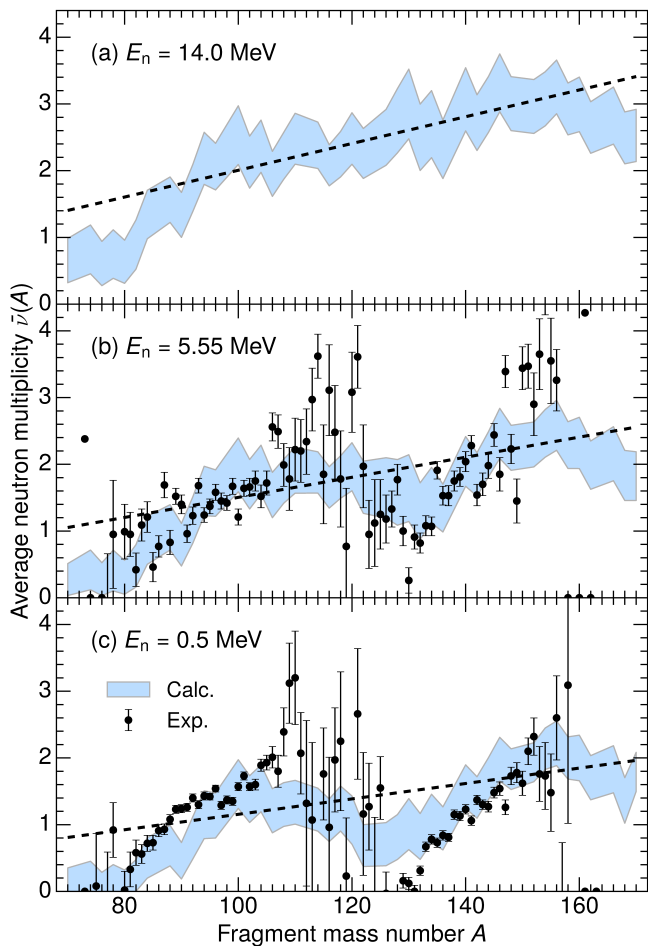


FIG. 4 (color online). For $^{235}\text{U}(n,f)$ is shown the mean neutron multiplicity as a function of the mass number of the primary fission fragment, $\bar{\nu}(A)$, for three different incident neutron energies E_n : 0.5 MeV (a), 5.55 MeV (b), 14 MeV (c). The calculated values are at the center of the light-blue shaded band which has a width equal to the calculated dispersion of the neutron multiplicity distribution for that fragment mass, $\sigma_\nu(A)$. The experimental data from Ref. [29] are also shown. The dashed line shows roughly the behavior resulting from an energy division according to mass.

energy in the mother fragment. For consistency, we employ the microscopic level density (3) for the evaporation daughter nucleus. Following the treatment in Ref. [28], the neutron evaporation is continued until the excitation energy has fallen below the neutron separation energy.

Figure 3 shows the calculated mean neutron multiplicity $\bar{\nu}(A)$ together with experimental data from a variety of experiments. The calculated $\bar{\nu}(A)$ is at the center of the light-blue band which has a width equal to the dispersion of the calculated neutron multiplicity distribution for that A , $\sigma_\nu(A)$. The band is shown to make it easier to identify the calculated value on the plot and, at the same time, to give a quantitative impression of the fluctuation in the number of neutrons emitted from a fragment.

The sawtooth appearance of the data is reasonably well reproduced by the calculation and arises from a combined effect of the behavior of the neutron separation energy $S_n(A)$, which displays a jump near $A = 132$ due to the closed shells at $Z = 50$ and $N = 82$, and the behavior of the total intrinsic fragment energy $E_{\text{dist}}(A) + E_{\text{sc}}^*(A)$ (see Fig. 2).

The energy dependence of the energy partitioning is illustrated in Fig. 4 which shows $\bar{\nu}(A)$ resulting from first-chance fission at three different incident neutron energies. The experimental data from Ref. [29] are also shown. The dashed line shows roughly the neutron multiplicity resulting if the excitation energy were divided according to the masses as suggested by the simple Fermi-gas level density. It is seen that the calculated results approach this behavior with increasing excitation energy. In the region around $A = 130$, the very low neutron multiplicity occurring for thermal fission grows rather rapidly with increasing neutron energy, causing the sawtooth feature of $\bar{\nu}(A)$ to become smoother. This behavior is due to the decrease of the strong negative shell correction at higher excitation energy for fragments in this mass region, increasing the level density and thus the share of the excitation energy taken up by the heavy fragment at scission.

In summary, in order to elucidate how the available excitation energy at scission is divided between the two fragments, we have augmented the recently developed level-density guided Metropolis shape evolution treatment [11] with shape-dependent microscopic level densities for the nascent fission fragments which are distorted relative to their equilibrium shapes. The available energy is partitioned statistically according to the corresponding microscopic level densities which take account of the structure effects in these distorted pre-fragments. For each fragment, the distortion energy is converted into additional excitation before they experience sequential neutron evaporation. The dependence of the resulting mean neutron multiplicity on fragment mass, $\bar{\nu}(A)$, agrees well with experimental data. In particular, the sawtooth appearance of $\bar{\nu}(A)$ can be understood from shell-structure effects in the level densities as well as from structure in the deformation energy surface.

We also studied how $\bar{\nu}(A)$ changes as the excitation energy of the fissioning nucleus is increased. The sawtooth behaviour is weakened due to the reduction of the shell corrections near $A = 130$ which significantly increases the level density in the heavy fragment and hence $\bar{\nu}$. Such an evolution is also seen in the experimental data.

It is noteworthy that the presented treatment stays within the well-established framework of the macroscopic-microscopic model of nuclear structure underlying the calculation of the nuclear potential-energy surfaces that have been used successfully to calculate fission-fragment mass distributions [9–11, 30]. This novel treatment has considerable predictive power and can readily be applied to other fission cases as well, including cases where no experimental data yet exist.

This work was supported by the Swedish Natural Science Research Council (S.Å.) and the Knut and Alice

Wallenberg Foundation (M.A., B.G.C. and S.Å.); J.R. was supported in part by the NNSA DNN R&D of the U.S. Department of Energy.

-
- [1] O. Hahn and F. Straßmann, *Naturwiss.* **27**, 11 (1939).
 [2] L. Meitner and O.R. Frisch, *Nature (London)* **143**, 239 (1939).
 [3] A. N. Andreyev, K. Nishio, and K.-H. Schmidt, *Rep. Prog. Phys.* **81**, 016301 (2018).
 [4] K.-H. Schmidt and B. Jurado, *Rep. Prog. Phys.* **81**, 106301 (2018).
 [5] N. Schunck and L. M. Robledo, *Rep. Prog. Phys.* **79**, 116301 (2016).
 [6] P. Talou *et al.*, *Eur. Phys. J. A* **54**, 9 (2018).
 [7] N. Bohr and J. A. Wheeler, *Phys. Rev.* **56**, 426 (1939).
 [8] H. A. Kramers, *Physica* **7**, 284 (1940).
 [9] J. Randrup and P. Möller, *Phys. Rev. Lett.* **106**, 132503 (2011).
 [10] J. Randrup, P. Möller, and A.J. Sierk, *Phys. Rev. C* **84**, 034613 (2011).
 [11] D. E. Ward, B. G. Carlsson, T. Døssing, P. Möller, J. Randrup, and S. Åberg, *Phys. Rev. C* **95**, 024618 (2017).
 [12] K. H. Schmidt and B. Jurado, *Phys. Rev. Lett.* **104**, 212501 (2010).
 [13] D. G. Madland and J. R. Nix, *Nucl. Sci. Eng.* **81**, 213 (1982).
 [14] S. Lemaire, P. Talou, T. Kawano, M. B. Chadwick, and D. G. Madland, *Phys. Rev. C* **72**, 024601 (2005).
 [15] N. V. Kornilov, F.-J. Hamsch, and A. S. Vorobeyev, *Nucl. Phys. A* **789**, 55 (2007).
 [16] H. A. Bethe, *Phys. Rev.* **50**, 332 (1936).
 [17] P. Möller, A. J. Sierk, T. Ichikawa, A. Iwamoto, R. Bengtsson, H. Uhrenholt, and S. Åberg, *Phys. Rev. C* **79**, 064304 (2009).
 [18] J. R. Nix, *Nucl. Phys. A* **130**, 241 (1969).
 [19] P. Möller, A. J. Sierk, and A. Iwamoto, *Phys. Rev. C* **92**, 072501 (2004).
 [20] H. Uhrenholt, S. Åberg, A. Dobrowolski, T. Døssing, T. Ichikawa, and P. Möller, *Nucl. Phys. A* **913**, 127 (2013).
 [21] K. Nishio, Y. Nakagome, H. Yamamoto, and I. Kimura, *Nucl. Phys. A* **632**, 540 (1998).
 [22] V. F. Apalin, Y. N. Gritsyuk, I. E. Kutikov, V. I. Lebedev, and L. A. Mikaelian, *Nucl. Phys. A* **71**, 553 (1965).
 [23] A. S. Vorobyev *et al.*, *EPJ Web Conf.* **8**, 3004 (2010).
 [24] O. I. Batenkov *et al.*, *AIP Conf. Proc.* **769**, 625 (2005).
 [25] J. W. Boldeman, A. R. de L. Musgrove, and R. L. Walsh, *Aust. J. Phys.* **24**, 821 (1971).
 [26] E. E. Maslin, A. L. Rodgers, and W. G. F. Core, *Phys. Rev.* **164**, 1520 (1967).
 [27] A. Göök, F. J. Hamsch, and S. Oberstedt, *EPJ Web Conf.* **169**, 4 (2018).
 [28] J. Randrup and R. Vogt, *Phys. Rev. C* **80**, 024601 (2009).
 [29] R. Müller, A. A. Naqvi, F. Käppeler, and F. Dickmann, *Phys. Rev. C* **29**, 885 (1984).
 [30] J. Randrup and P. Möller, *Phys. Rev. C* **88**, 064606 (2013).